

Original article

Diffusional Monte Carlo model of liquid-phase sintering

A. Luque^{a,*}, J. Aldazabal^a, J.M. Martínez-Esnaola^a, A. Martín-Meizoso^a,
J. Gil Sevillano^a, R.S. Farr^{b,c}

^a CEIT and Tecnun (University of Navarra), Manuel Lardizábal 15, 20018 San Sebastián, Spain

^b Unilever R&D Colworth House, Sharnbrook, MK44 1LQ Bedford, United Kingdom

^c London Institute for Mathematical Sciences, 22 South Audley St., Mayfair, W1K 2NY London, United Kingdom

Received 29 November 2010; received in revised form 12 April 2011; accepted 11 May 2011

Available online 20 May 2011

Abstract

Liquid-phase sintering (LPS) is a consolidation process for metallic and ceramic powders. At given temperature conditions, the process occurs with constant amount of liquid phase. However, the evolution of solid-particle shape is observed, namely, the rounding of particles and the growth of big particles at the expense of the small ones, which is known as Ostwald ripening.

In this work, we propose a Monte Carlo (MC) model to simulate the microstructural evolution during LPS. The model considers the change of state of the discretising elements, namely voxels, of the system. The microstructural evolution proceeds accounting for both the geometrical characteristics of the particles, such as the number of solid neighbours, and the amount of solute contained in or surrounding a randomly chosen voxel. This has been implemented in terms of two probability distribution functions (PDFs). The diffusion of solute has also been considered by means of the implementation of a three-dimensional finite-difference algorithm.

The diffusional MC model that we present is able to reproduce the Ostwald ripening behaviour and, in particular, results match the case in which the process is limited by the diffusion of the solute in the liquid phase.

© 2011 IMACS. Published by Elsevier B.V. All rights reserved.

Keywords: Liquid-phase sintering; Ostwald ripening; Monte Carlo model; Probability distribution function; Diffusion limited kinetics

1. Introduction

The present work is a follow-up of the work presented in Ref. [15]. In that work, we first made a brief description of multi-scale computational modelling, paying special attention to the micro-scale techniques, in which the Monte Carlo (MC) method is included. Then, we introduced the concept of sintering, in general, and the particularities of liquid-phase sintering. We summarized the theoretical background of these processes and included the main assumptions to tackle the problem of particle coarsening, either by Ostwald ripening [19] or by particle coalescence, from an analytical point of view. Finally, the geometrical MC model of liquid-phase sintering was defined. After that, the method was validated and some simulation results were shown.

In this article, we propose a MC method that combines the geometrical MC model of Ref. [15] with a diffusional MC model, in order to take into account the presence of a solute and its diffusion through the liquid phase. The main

* Corresponding author at: CEIT and Tecnun (University of Navarra), Department of Materials, Manuel Lardizábal 15, 20018 San Sebastián, Spain. Tel.: +34 943212800; fax: +34 943213076.

E-mail address: aluque@ceit.es (A. Luque).

Table 1

Weights assigned to different types of neighbours, to determine the normalised number of solid neighbours of a voxel, in the geometrical model [1].

| Neighbour type | Number | Weight | Normalised weight |
|----------------|--------|-------------------|---------------------|
| Face | 6 | 1 | $(\sqrt{2} - 1)/6$ |
| Edge | 12 | $1/\sqrt{2}$ | $(2 - \sqrt{2})/12$ |
| Vertex | 8 | 0 | 0 |
| Max. weight | | $6(1 + \sqrt{2})$ | 1 |

features of the geometrical model will be summarized below (see Section 2) for clarity. Once the method is defined and validated, some results obtained using the proposed complete model will be shown.

2. Geometrical MC model of LPS

The computer models of LPS presented in Ref. [15] and the model that we will present here are based on the Monte Carlo (MC) technique. This technique consists of the random modification of the elements that form the system [18]. Thus, the simulated microstructures have to be divided into volume elements, called “voxels”, which, in this work, are cubes of constant size, although other microstructural discretisation shapes (for instance, tetrakaidecahedra [17]) could be used. This is one of the advantages of this type of models compared to other Ostwald ripening and sintering models [3] which are merely analytical. We can obtain not only the overall behaviour (evolution of the mean particle radius or evolution of the particle distribution, for instance), but also the evolution of some local characteristics (particle topology, neck growth) during sintering.

For the geometrical MC model, a state is assigned to each voxel. In the simulations that were carried out, that state can be “solid” or “liquid”. The modification of the voxels is done according to a previously defined probability distribution function (PDF). Thus, the proposed PDF tries to capture the physics of the process in terms of voxel state and, particularly, particle curvature. Instead of measuring the actual curvature of the particle, we proposed a modification of the intersection method [20], based on the number of solid or liquid voxels that surround a certain voxel, to obtain an equivalent curvature.

In the proposed method, only first-neighbours are considered and these neighbours are given different weights to modify their influence according to the different voxel types. These weights are assumed to depend on the inverse of the distance between the centres of two voxels, as shown in Table 1[1].

The model tries to modify the state of one voxel of the system at a time. For instance, if a liquid voxel is chosen during the simulation, the normalised number of solid neighbours, n_S , is computed. We can intuitively see that the solidification of the liquid voxel is more likely to happen when that parameter is close to 1. The eventual solidification depends on the corresponding geometrical probability distribution function (G-PDF), as a function of n_S . These probability functions are constructed taking into account certain features, summarized in Ref. [15]. The G-PDF for solidification, $p_S^G(n_S)$, is defined as (see Fig. 1):

$$p_S^G(n_S) = \begin{cases} 4n_S^3, & 0 \leq n_S \leq 1/2 \\ 1 - 4(1 - n_S)^3, & 1/2 < n_S \leq 1 \end{cases} \quad (1)$$

When all the voxels of the system of the MC simulation have been chosen once on average, we say that the simulation time has increased by 1 Monte Carlo step (MCS).

3. Diffusional MC model of LPS

As mentioned, the diffusional model that we propose is also based on the Monte Carlo technique, and therefore, it benefits from the advantages of tackling with a discretised system and a real distribution of particles, compared to other analytical models [14,30,3]. Nevertheless, in this case, voxels are assigned not only a state (“solid” or “liquid”) but also a new parameter, namely the solute concentration, which represents the amount of solute contained in the voxel, ranging between 0 and 1. Therefore, this new characteristic of the voxels has to be accounted for, apart from the number of solid neighbours, in order to proceed with the microstructural evolution. This is, in fact, the first advantage

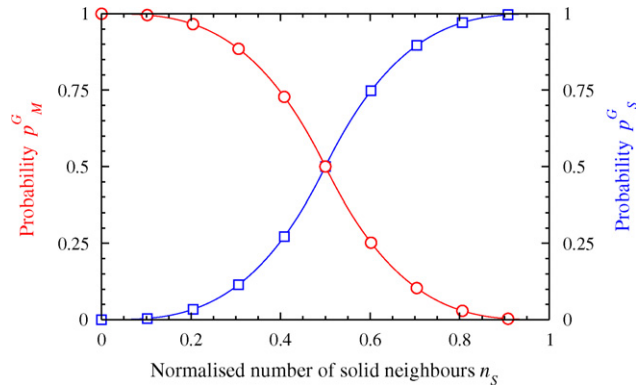


Fig. 1. Geometrical probability distribution functions, p_M^G (circles) and p_S^G (squares), for the melting and the solidification processes, respectively, as a function of the normalised number of solid neighbours, n_s .

of the proposed model compared to other existing alternative models of Ostwald ripening and sintering [25,26,12], which are purely geometrical and do not consider a second component in the simulations. Besides the MC model that we propose in this work has the advantage over phase field models, such as that in Ref. [11], that the interface between solid and liquid in our model is less diffuse and, hence, it is sharply defined, which reduces the required number of voxels in a simulation.

In the same manner as for the geometrical MC model, the equivalence between simulation length and real length, x_L , is freely chosen. Voxels can be considered as coarse-grained entities consisting of many atoms. But there is not a unique value for x_L and, hence, it can be arbitrarily chosen. However, the equivalence between simulation time and real time, x_t , would depend on the values of the diffusion coefficient, D , and the solid/liquid surface energy, γ . If we choose the values of x_L and D , which also depends on T , then, the value of x_t is set. Besides, if we generate a particular PDF to deal with solute concentration, which indirectly establishes the value of γ , the characteristics of the model, in general, and the ripening rate, κ , in particular, are determined, and so is the deviation from the ideal Ostwald ripening process. As we are considering the diffusion of one of the present species, we can also simulate a diffusion-limited process.

The model is applicable to any system in which the change of volume on solidification and on mixing of the two liquid components is negligible. In this work, we have simulated a binary system composed of silicon and aluminium. Apart from the technological interest of this alloy, the reason why these two elements have been chosen is the small difference in their densities. At room temperature, the density of silicon is 2330 kg m^{-3} and the density of aluminium is 2700 kg m^{-3} [13]. Therefore, we can neglect the change of volume during solidification or melting of the silicon, and also volume and mass fractions in this system can be treated interchangeably, which aids in the interpretation of the results. The corresponding phase diagram can be seen in Fig. 2. The distinctive feature of the Si–Al system is that, in

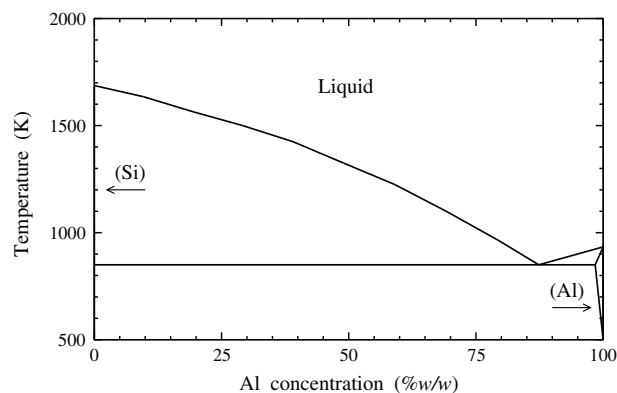


Fig. 2. Silicon–aluminium phase diagram, as a function of the weight percentage of Al.

the whole range of temperatures, silicon admits very little aluminium in its lattice (less than 15 ppm). For this reason, above 850 K, a binary system of these components would be formed by solid Si, with almost no Al in solid solution, and a liquid phase, with varying aluminium concentration according to the *liquidus* line. The amount of each phase can be determined by means of the inverse lever rule. For instance, to determine the weight fraction of liquid, f_w^{liq} , we have to apply:

$$f_w^{liq} = \frac{c - c_{sol}(T)}{c_{liq}(T) - c_{sol}(T)} \quad (2)$$

where c is the aluminium concentration in the system, $c_{liq}(T)$ is the minimum amount of aluminium that the liquid can contain at a given temperature and $c_{sol}(T)$ is the maximum amount of aluminium that silicon can contain at a given temperature. As mentioned, in the case of the Si–Al system, $c_{sol} \simeq 0$.

Note that the phase diagram yields weight fractions and that our simulations can be most easily characterised in terms of volume fractions, which can directly be calculated from the simulations. Nevertheless, neglecting the change of volume during solidification or melting of the silicon, which for the case of Al and Si is small, the volume fraction number and the weight fraction number coincide. Besides, we will assume volume additivity so that the density of a liquid mixture of Al and Si is not very different from the densities of the pure components.

3.1. Model definition

Although particle curvature is important for microstructural evolution, diffusion has to be taken into account because the diffusional process of the solute (in this work, aluminium) is relevant to some real systems [4,5,7–9,22–24,28,31,32]. For this reason, aluminium concentration of liquid voxels, ranging between 0 and 1, and the subsequent aluminium diffusion are included in the model proposed in this work, which is thus more than purely geometric. Nevertheless, the limiting step of the process could still be the attachment and the detachment of atoms (this is to say, the diffusion of aluminium might be much faster than the attachment kinetics). However, the presence of that solute in the system, on one hand, and the necessity of moving aluminium away from the silicon interface before more liquid can be attached to the particle, on the other hand, can make the Ostwald ripening process turn from reaction-limited into diffusion-limited ($D \ll R\xi$, where R is the particle radius and ξ is the reaction rate) [14,30]. Note that, for Ostwald ripening to proceed, silicon has to be available around solid Si particles so it attaches to them. But if the diffusion of aluminium is not fast enough, this species will fill the surrounding of the Si particle, and that will avoid the solidification process, as we will see later.

The introduction of a solute into the simulations involves considering the phase diagram of the components and implementing the diffusion of this species. At a given temperature, the amount of solute in the liquid in equilibrium with a flat solid interface is called c_e and that value can be determined according to the *liquidus* line. In this work, we have arbitrarily set $T = 1375$ K, but another temperature could be chosen. The aluminium concentration in the liquid in equilibrium with the solid at the chosen temperature is $c_e = 44\%$ w/w, but note that, if a different temperature were chosen, then c_e would change. Despite c_e being constant for a given temperature, the liquid can contain more or less solute. If the liquid contains more solute than the amount given by the phase diagram, it is said to be “saturated” or “supersaturated”. In fact, as expressed by Thomson–Freundlich’s equation, the equilibrium concentration around a particle, namely c_R , varies as a function of $1/R$ (the curvature of the particle) as

$$c_R = c_e \exp\left(\frac{2\gamma\Omega}{k_B T} \frac{1}{R}\right) \quad (3)$$

where c_R is the solute concentration at the surface of a particle of radius R , Ω is the atomic volume and k_B is Boltzmann’s constant. Therefore, for the case of the binary system considered in this work, the higher the local curvature of a solid Si particle, the higher the Si amount and the lower the Al amount that is in local equilibrium with that particle. Then, if the real amount of Al surrounding the particle is higher than the value at equilibrium, the solid Si particle tends to melt, and *vice versa*.

As for the geometrical MC model, we avoid measuring the local curvature in the voxelized microstructure. Instead, we propose to calculate an equivalent curvature, based on the concentration of the surrounding voxels: the average concentration, c_{ave} , of the liquid voxels surrounding a certain voxel. The expression of c_{ave} is different depending on

the voxel state and only liquid first-neighbours are taken into account. For a solid voxel, the average concentration is calculated as

$$c_{ave} = \frac{\sum_{liq} w_j c_j}{\sum_{liq} w_j} \tag{4}$$

where w_j is a factor introduced to take into account the type of neighbour (face, edge or vertex neighbour), calculated as the inverse of the square of the distance between two voxel centres. For a liquid voxel of concentration c_i , the average concentration is

$$c_{ave} = \frac{c_i + \sum_{liq} w_j c_j}{1 + \sum_{liq} w_j} \tag{5}$$

As we can see, the only difference between Eqs. (4) and (5) is that the concentration of the liquid voxel itself is accounted for, when computing the average concentration of that liquid voxel.

Similarly to the geometrical MC model, the occurrence of either the solidification or the melting process depends on the corresponding concentration-dependent probability distribution functions (C-PDFs), given as functions of c_{ave} . Several constraints apply when constructing these probabilities. Calling the C-PDF for solidification and melting p_S^C and p_M^C , respectively, then $0 \leq p_S^C, p_M^C \leq 1$, for all the possible values of c_{ave} . Particularly if $c_{ave} = c_e$, $p_S^C = p_M^C$. In fact,

$$p_S^C(c_{ave}) + p_M^C(c_{ave}) = 1 \tag{6}$$

Therefore, $p_S^C(c_e) = p_M^C(c_e) = 0.5$. Finally, considering the cumulative probabilities of both p_S^C and p_M^C , it must be ensured that

$$\int_0^1 p_S^C(c_{ave}) dc_{ave} = \int_0^1 p_M^C(c_{ave}) dc_{ave} = \frac{1}{2} \tag{7}$$

In this work, the C-PDF for melting, $p_M^C(c_{ave})$, at the arbitrarily chosen temperature of 1375 K ($c_e = 44\%$ w/w Al), is defined as follows:

$$p_M^C(c_{ave}) = \begin{cases} \alpha_1 + \alpha_2 c_{ave} + \alpha_3 c_{ave}^2 + \alpha_4 c_{ave}^3, & 0 \leq c_{ave} \leq c_e \\ \alpha_5 + \alpha_6 (1 - c_{ave}) + \alpha_7 (1 - c_{ave})^2 + \alpha_8 (1 - c_{ave})^3 + \alpha_9 (1 - c_{ave})^4, & c_e < c_{ave} \leq 1 \end{cases} \tag{8}$$

where the values of the constants can be analytically expressed in terms of c_e as

$$\begin{aligned} \alpha_1 &= 0 & \alpha_5 &= 1 \\ \alpha_2 &= 0 & \alpha_6 &= 0 \\ \alpha_3 &= 1.5(1 - 2c_e)c_e^{-2} & \alpha_7 &= 1.5(9 + c_e)(2c_e - 1)(1 - c_e)^{-3} \\ \alpha_4 &= (3c_e - 1)c_e^{-3} & \alpha_8 &= -(3c_e^2 + 55c_e - 28)(1 - c_e)^{-4} \\ & & \alpha_9 &= 15(2c_e - 1)(1 - c_e)^{-5} \end{aligned} \tag{9}$$

Fig. 3 shows the C-PDF for both solidification and melting, as a function of the average concentration, c_{ave} . The constructed C-PDF has been chosen among different possibilities taking into account the aforementioned conditions. The shape of these functions is not simply sigmoidal because some extra constraints, such as the values of the derivatives of p_M^C or p_S^C at $c_{ave} = 0$, $c_{ave} = c_e$ and $c_{ave} = 1$, were also imposed. The obtained C-PDF for the temperature of 1375 K, whose expression is given by Eq. (8) with coefficients given by Eq. (9) and which is shown in Fig. 3, gives the best performance in terms of the established criteria [15], both qualitatively (faceting and roughness) and quantitatively (spherically symmetric behaviour, Y_i , and surface roughness, $\sigma_R(\mu_R)$). Y_i is a parameter which measures the deviation

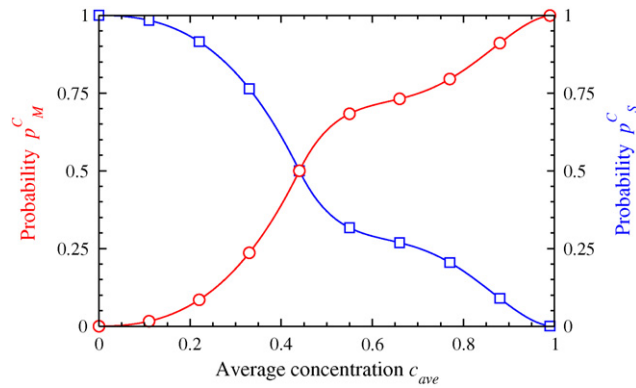


Fig. 3. Concentration-dependent probability distribution functions, p_M^C (circles) and p_S^C (squares), for the solidification and the melting processes, respectively, as a function of the average concentration, c_{ave} .

of the particle shape from a sphere, and is sensitive specifically to deviations which satisfy cubic/octahedral symmetry [15]. The values of Y_i corresponding to a sphere, a cube and an octahedron are 0, 0.344 and -0.278 , respectively. $\sigma_R(\mu_R)$ represents the surface roughness of the particle and is measured in terms of the standard deviation of the distances between the particle surface and its centre as a function of the mean distance from the centre of the particle to its surface [15].

Naturally, the concentration-dependent probability distribution functions are key parameters in the model. A different choice in the temperature, which affects the value of c_e , would have changed the value of the coefficients appearing in Eq. (8). But obtaining the new coefficients is a straightforward process. A different choice in the system components, with the aforementioned restrictions, would have had the same effect: for a given T , the value of c_e would have been different and, hence, the expression of the C-PDF would have changed. Finally, note that the particle shape or the particle size is not involved in the calculation of the coefficients appearing in the C-PDF.

Nevertheless, in the diffusional MC model, not only the C-PDFs are important. Another key question is the proportion of aluminium collected from or expelled to the surrounding liquid voxels, when a silicon voxel melts or a liquid voxel solidifies, respectively. On one hand, if a liquid voxel of concentration c_i solidifies, the amount of aluminium expelled to each one of the neighbouring liquid voxels is

$$\Delta c_j = \frac{c_i w_j / c_j}{\sum_{\text{liq}} w_k / c_k} \tag{10}$$

Eq. (10) implies that the Al amount expelled to a neighbouring liquid voxel is inversely proportional to the square of the distance between the voxels and to the concentration of the target liquid voxel. Note that, in the solidification process, the amount of aluminium remains constant as the total amount of Al expelled to the liquid neighbours from a liquid voxel of concentration c_i about to solidify is, precisely, c_i . On the other hand, if a solid voxel melts, the amount of aluminium collected from each one of the neighbouring liquid voxels is

$$\Delta c_j = \frac{c'_{ave} w_j c_j}{\sum_{\text{liq}} w_k c_k} \tag{11}$$

where c'_{ave} is the concentration of the solid voxel once it has melted, calculated as

$$c'_{ave} = \frac{\sum_{\text{liq}} w_j c_j}{1 + \sum_{\text{liq}} w_j} \tag{12}$$

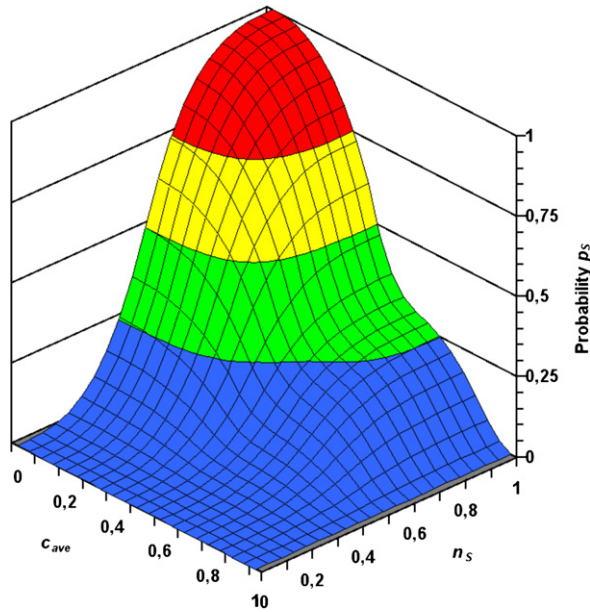


Fig. 4. Probability distribution function for the solidification process, p_s , as a function of the normalised number of solid neighbours, n_s and the average concentration, c_{ave} .

Eq. (11) implies that the Al amount collected from a neighbouring liquid voxel is proportional to its concentration and inversely proportional to the square of the distance between the voxels. Note that, in the melting process, the amount of aluminium remains constant as the total amount of Al collected from the surrounding liquid voxels and collected by the solid voxel about to melt is, precisely, c'_{ave} . The way for calculating the average concentration (Eqs. (4) and (5)) and for assigning the aluminium amount expelled to (Eq. (10)) and collected from (Eq. (11)) the surrounding voxels is not unique and, in this work, has been established after trying several alternatives. These expressions correspond to options which ensure that $0 \leq c \leq 1$, during the simulation.

Combining both the G-PDFs and the C-PDFs, we calculate the total probability of solidification of a liquid voxel as

$$p_s(n_s, c_{ave}) = p_s^G(n_s) \times p_s^C(c_{ave}) \tag{13}$$

This implies that, for the eventual solidification of a liquid voxel, it has to pass the test of a combination of G-PDF and C-PDF, and not of each one separately (“conditioned probability”). Nevertheless, the selection of a “joint probability” has been verified to be not determinant to the simulation results. Fig. 4 shows the resulting PDF for solidification as a function of n_s and c_{ave} . The total probability of melting of a solid voxel is calculated with an expression analogous to that given in Eq. (13).

Finally, we explain how the diffusion process is implemented in the proposed model. Solute diffusion takes place as a consequence of Fick’s first law. Besides, Fick’s second law provides the temporal evolution of the concentration at any point of the system. Assuming that the Al diffusion coefficient does not depend on the concentration, and using Cartesian coordinates, Fick’s second law can be written as

$$\frac{\partial c}{\partial t} = D \left(\frac{\partial^2 c}{\partial x^2} + \frac{\partial^2 c}{\partial y^2} + \frac{\partial^2 c}{\partial z^2} \right) \tag{14}$$

On the one hand, we do not know the analytical dependence of c on position and time. On the other hand, the simulation system is not continuous, as it has been discretised. Time is also discretised into “attempts” to modify the state of a voxel and, eventually, into MCSs. For these reasons, we choose to solve Eq. (14) applying an explicit finite-difference technique [1,21], and making use of the corresponding approximations for $\partial c/\partial t$, $\partial^2 c/\partial x^2$, $\partial^2 c/\partial y^2$ and $\partial^2 c/\partial z^2$, for voxel i at coordinates (x_i, y_i, z_i) and time t . This technique yields that the concentration of voxel i at time $t + \Delta t$ can be

explicitly expressed in terms of the concentration of the voxel and the concentration of the face neighbours at time t as

$$c(x_i, y_i, z_i, t + \Delta t) = c(x_i, y_i, z_i, t) + \frac{D\Delta t}{\Delta x^2} (c(x_i + \Delta x, y_i, z_i, t) + c(x_i, y_i + \Delta y, z_i, t) + c(x_i, y_i, z_i + \Delta z, t) - 6c(x_i, y_i, z_i, t) + c(x_i - \Delta x, y_i, z_i, t) + c(x_i, y_i - \Delta y, z_i, t) + c(x_i, y_i, z_i - \Delta z, t)) \quad (15)$$

where Δt is precisely the time between diffusion steps and $\Delta x = \Delta y = \Delta z$ is the voxel size. Note that, for real systems, D depends on the process temperature. Nevertheless, it is convenient to define the dimensionless parameter \tilde{D} as

$$\tilde{D} = \frac{D\Delta t}{\Delta x^2} \quad (16)$$

Varying the value of \tilde{D} , we are able to simulate different diffusivities (the higher its value, the faster the diffusion) and, hence, we can capture the dependence of this variable on T . However, a linear-stability analysis of Eq. (15) yields that \tilde{D} can only range between 0 and 1/6 (Courant's condition [21]). Otherwise, a liquid voxel could have an aluminium concentration lower than 0 or greater than 1, after a diffusion step. In this work, we will use $\Delta t = 1$ MCS and $\tilde{D} = 0.1$. The diffusion algorithm has been tested in previous works [1]. Note that the value of \tilde{D} ($0 \leq \tilde{D} \leq 1/6$) has to be such that, on one hand, the saturation of the voxels of the interface and, hence, dendritic growth are avoided and, on the other hand, a very fast movement of aluminium from the interface is not permitted. As mentioned in the beginning of the paper, this parameter would permit simulating Ostwald ripening in different regimes: from the reaction- to the diffusion-limited case.

The constructed C-PDFs and the diffusional parameters need to be checked before carrying out simulations with this model. Clearly, we can use the criteria proposed for the geometrical MC model, namely the faceting and surface roughness parameters. But as aluminium diffusion has been introduced into the model and the Si–Al phase diagram has been considered, new criteria, more appropriate for this model, could be established.

- The first one is the number of liquid voxels trapped within the solid, especially during solidification. This number should be as small as possible, and preferably zero. The number of trapped voxels may indicate an inadequate solidification process.
- The second one is the evolution of the solid volume fraction in the system. Note that the simulations carried out in this work are isothermal and, hence, they should reach a constant amount of solid, given by the phase diagram according to the solute concentration. This parameter is particularly important in those simulations which start with the Si solid fraction at equilibrium with the amount of Al.

Finally, the boundary conditions applied to the systems simulated with the diffusional MC model are periodic boundary conditions (PBCs) along the x -, the y - and the z -axis, in order to minimise edge effects.

3.2. Model validation

The validation of the proposed C-PDFs (Eq. (8) and Fig. 3), in combination with the proposed G-PDFs (Eq. (13) and Fig. 4) is done by carrying out two simulations in which the initial solid fraction is out of equilibrium with the amount of aluminium present in the system, according to the Si–Al phase diagram.

We generate two systems of the same size, namely, $50 \mu\text{m} \times 50 \mu\text{m} \times 50 \mu\text{m}$. In the first system, we place a spherical particle of $20 \mu\text{m}$ of diameter. In the second one, the diameter of the particle is $48 \mu\text{m}$. The initial solid volume fractions are 3.4% and 46.3%, respectively (according to the phase diagram, at 1375 K, these fractions can be obtained when the total Al contents of the system are 42.5% w/w and 23.6% w/w, respectively). Thus, a total of 23.6% w/w aluminium is placed in the first system and the aluminium concentration in each liquid voxel is 24.4% w/w. The difference between this value and the equilibrium value ($c_e = 44\%$ w/w Al, at 1375 K) produces the particle growth (solidification). Analogously, we put a total of 42.5% w/w Al in the second system and the aluminium concentration in each liquid voxel is 79.1% w/w. Again, the difference between this value and c_e produces the particle melting. The parameter x_L is equal to $1 \mu\text{m}/\text{voxel}$. Fig. 5 shows the evolution of the sphericity, Y , and the surface roughness, σ_R ,

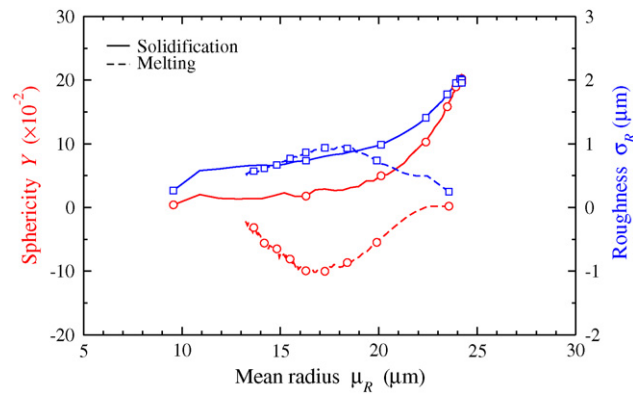


Fig. 5. Sphericity, Y (circles), and surface roughness, σ_R (squares), as a function of the mean radius, μ_R , obtained during the simulations of solidification (continuous line) and melting (dashed line), with the diffusional model. Note that Y equals 0 for a sphere, 0.344 for a cube and -0.278 for an octahedron.

as a function of mean radius, μ_R , during the simulations. No liquid voxels remain trapped within the solid particles throughout these simulations.

If we look at the simulations carried out with the diffusional model, we can observe that, unless neck formation takes place, Si particles remain rather spherical, according to the values of Y and σ_R . However, results are now slightly worse, especially during solidification, compared with those obtained with the geometrical model [15]. On the one hand, during melting, particle sphericity is lost, but it is recovered when the solid volume fraction gets closer to the equilibrium value, as shown in the change of tendency for $\mu_R < 15 \mu\text{m}$ (see Fig. 5). On the other hand, the solidification occurs faster than the diffusional process. For this reason and due to the periodic boundary conditions imposed, for the biggest value of μ_R , as shown in Fig. 5, Y is about 0.2 (approximately the value of Y for a cube, see Fig. 6) and $\sigma_R \simeq 2 \mu\text{m}$, which indicate an incipient dendritic growth. Nevertheless, when the equilibrium amount of solid is reached ($\mu_R \simeq 24 \mu\text{m}$), both Y and σ_R start to decrease. Hence, the particle starts to become rounder and smoother. It is important to note that, as particles remain nearly spherical, especially in conditions close to the equilibrium, we can calculate the equivalent radius from its volume.

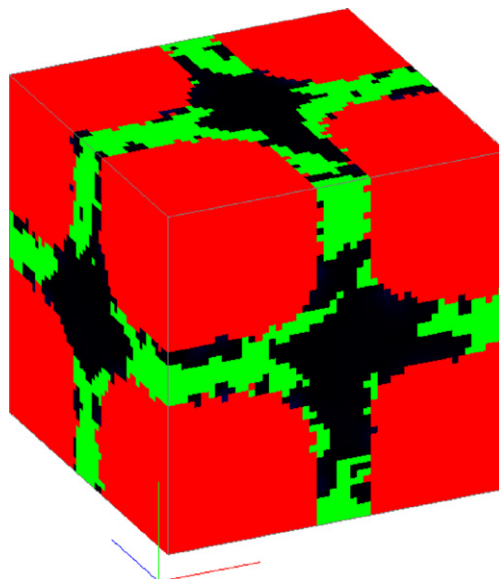


Fig. 6. System configuration during the test of the solidification process with the diffusional model. The somewhat cubic shape of the particle is due to rapid growth compared with slow diffusion. Red voxels represent the solid and green voxels are supersaturated voxels ($c > 44\%$, w/w, Al). (For interpretation of the references to color in this figure legend, the reader is referred to the web version of the article.)

Table 2

Initial equivalent radii of the particles for simulating the Ostwald ripening process and the sintering, with the diffusional model.

| ID | R_1 (μm) | R_2 (μm) | Initial f_{vol} (%) | Initial contact |
|--------|-------------------------|-------------------------|-----------------------|-----------------|
| Sim. 1 | 4.3 | 13.0 | 15 | No |
| Sim. 2 | 7.5 | 15.0 | 25 | No |
| Sim. 3 | 5.2 | 15.4 | 25 | No |
| Sim. 4 | 3.9 | 15.6 | 25 | No |
| Sim. 5 | 5.8 | 17.3 | 35 | No |
| Sim. 6 | 12.4 | 12.4 | 25 | Yes |

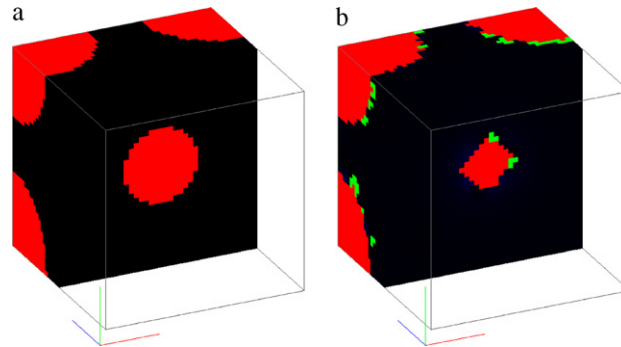


Fig. 7. Microstructural evolution in Sim. 2 (see Table 2 for identification of the simulation) during Ostwald ripening with the diffusional model, at (a) $t=0$ and (b) $t=1000$ MCS. Red voxels represent the solid and green voxels are supersaturated voxels ($c > 44\%$, w/w, Al). (For interpretation of the references to color in this figure legend, the reader is referred to the web version of the article.)

3.3. Ostwald ripening simulations

Once the diffusional model has been validated, we proceed to study how the C-PDFs reproduce the Ostwald ripening. For that, we carry out a total of five simulations. In all of the cases, the system size is $40 \mu\text{m} \times 40 \mu\text{m} \times 40 \mu\text{m}$. In the system, we place two particles of different sizes, as summarized in Table 2. Again, $x_L = 1 \mu\text{m}/\text{voxel}$. Fig. 7 shows the state of the system in Sim. 2 at $t=0$ and $t=1000$ MCS. In Fig. 8, the solid volume fraction of the system, f_{vol} , during the Ostwald ripening simulations with the diffusional model, can be observed. We can observe that the fraction of solid decreases at the beginning of the simulation. Due to the initial homogeneous distribution of aluminium, the amount of Al at the Si-matrix interface is higher than the amount at equilibrium, given by Eq. (3). Therefore, silicon particles melt partially and “temporally”, while Al is redistributed.

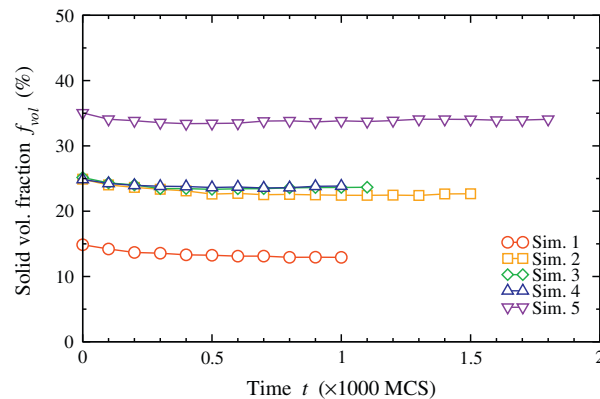


Fig. 8. Temporal evolution of the solid fraction of the system, f_{vol} , during the Ostwald ripening simulations with the diffusional model (see Table 2 for identification of the simulations).

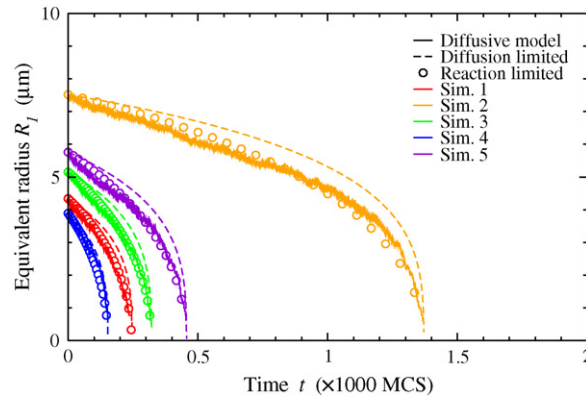


Fig. 9. Temporal evolution of the equivalent radius of the smallest particles of the system, during the Ostwald ripening simulations with the diffusional model (continuous lines). The results obtained applying the Ostwald ripening theories in the diffusion-limited case (dashed line) and the reaction-limited case (circles) are also shown (see Table 2 for identification of the simulations).

Fig. 9 shows the temporal evolution of the equivalent radius of the smallest particle in each system. As in the geometrical model, the power-law relationship between \bar{R} and t for the particle distribution, as predicted by the Ostwald ripening theories, does not apply to just two particles. However, we can apply Eqs. (17) and (18), corresponding to the classic Ostwald ripening theories, to the case of two particles. This permits us to compare the results obtained with the diffusional model and those obtained theoretically for well separated particles (diffusion limited kinetics, Eq. (17), and reaction limited kinetics, Eq. (18)). For this comparison, the time axis has been scaled so that the moment when the smallest particle of the system disappears coincides in each of the cases.

$$\frac{dR}{dt} = \frac{2\gamma\Omega^2 c_e D}{k_B T} \frac{D}{R} \left(\frac{1}{\bar{R}} - \frac{1}{R} \right) \quad (17)$$

$$\frac{dR}{dt} = \frac{2\gamma\Omega^2 c_e}{k_B T} \xi \left(\frac{\bar{R}}{R^2} - \frac{1}{R} \right) \quad (18)$$

Considering the diffusional model, however, the prediction of the LSW theory is not matched, as shown in Fig. 9. The (rescaled) reaction-limited Ostwald ripening result is surprisingly closer to the simulation results. Nevertheless, we have to bear in mind the differences between our model and the LSW theory: we are dealing with non-zero solid fractions, which lead to finite separations between the particles, in systems that are not under steady-state conditions. Non-zero solid fractions also produce a faster ripening process. Besides, the mean field nature of Ostwald ripening gives rise to local effects during the simulations, which eventually produce deviations from the theoretical predictions. Thus, ideally, we should compare our computational results with available experimental results (at these Al concentration and temperature conditions) and with other analytical approaches without the mentioned limitations of the LSW theory (cf. Refs. [2,4,8,16,27–29,33]). However, most of these theories lack an analytical expression for the evolution of the particle size and, hence, that makes the comparison difficult.

3.4. Neck formation and growth simulations

In the following, we analyse how the diffusional model deals with the sintering process. For that, we carry out a new simulation. The system size is $40 \mu\text{m} \times 40 \mu\text{m} \times 40 \mu\text{m}$. In the system, we place two particles of the same size, as shown in Table 2 for Sim. 6. In this case, particles are initially touching. Fig. 10 shows the system configuration in Sim. 6 at $t=0$ and $t=500$ MCS.

Fig. 11 shows a double-logarithmic representation of the temporal evolution of the neck size, $2X$, and \bar{F}_{geom} , during Sim. 6 (neck formation and growth). As particles are no longer spherical, due to the presence of the neck, we require the parameter \bar{F}_{geom} to measure their size. This parameter is based on the definition of F_{geom} :

$$F_{geom} = \sqrt{F_{long} F_{short}} \quad (19)$$

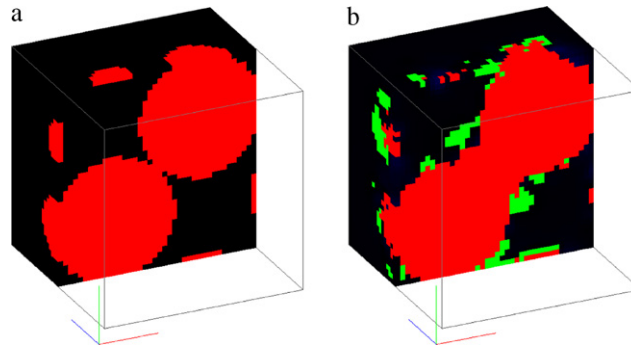


Fig. 10. Microstructural evolution in Sim. 6 (see Table 2 for identification of the simulation) during neck growth with the diffusional model, at (a) $t=0$ and (b) $t=500$ MCS. Red voxels represent the solid and green voxels are supersaturated voxels ($c > 44\%w/w$ Al). (For interpretation of the references to color in this figure legend, the reader is referred to the web version of the article.)

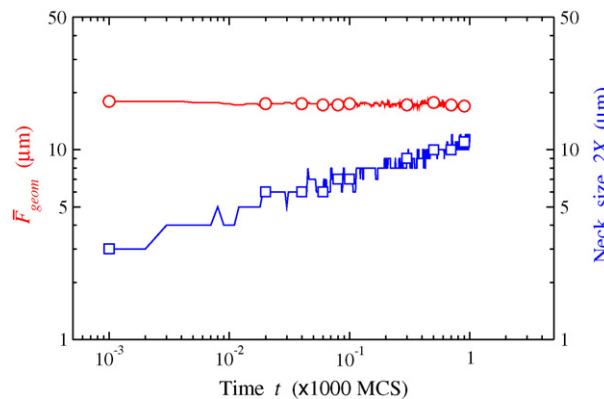


Fig. 11. Double-logarithmic plot of the temporal evolution of \bar{F}_{geom} (circles) of the particles that form the system, and the neck size, $2X$ (squares), during the sintering simulation with the diffusional model.

where F_{long} and F_{short} are the longest and the shortest Feret’s diameter of a particle, hence \bar{F}_{geom} being the arithmetic mean of the values of F_{geom} of the particles that form the neck.

The exponents of the power-law fits of the curves in Fig. 11 are summarized in Table 3. We can see that the value of \bar{F}_{geom} can be regarded as constant all along the simulation. This is one of the assumptions made for deriving the analytical solutions of neck growth during particle coalescence [15]. Besides, the slope of $\ln(2X)$ vs. $\ln(t)$ is also constant during the simulation. However, the calculated exponents of the dependence of $2X$ on t are different, if we consider the two developed models. As summarized in Table 3, the measured exponent has a value between $1/6$ and $1/5$ for the diffusional model, whereas it was approximately equal to $1/4$ for the geometrical MC model [15]. Therefore, the type of process that we are dealing with (either reaction-limited or diffusion limited) is changing the speed of the neck growth. Obviously, the absence of Al in the geometrical model permits a faster growth of the neck ($2X \propto t^{1/4}$ vs. $2X \propto t^{1/6}$). While the neck grows, Al has to move away from the region in order to allow further growth. On the other hand, we can compare the result of the diffusional model with other available theories, such as Courtney’s [6] and Farr’s [10] theories.

On the one hand, Fig. 12a shows the evolution of the reduced neck size, $x = X/\bar{F}_{geom}$, with the scaled time, t/\bar{F}_{geom}^3 , and the predictions corresponding to Courtney’s theory [6]. We can observe that the simulation result lies between

Table 3
Exponents of the power-law fits of $2X$ and \bar{F}_{geom} as a function of t , for the sintering simulation with the diffusional model.

| ID | Exponent of $2X$ vs. t | Correl. coeff. (%) | Exponent of \bar{F}_{geom} vs. t | Correl. coeff. (%) |
|--------|--------------------------|--------------------|--------------------------------------|--------------------|
| Sim. 6 | 0.186 | 94.8 | −0.003 | 98.5 |

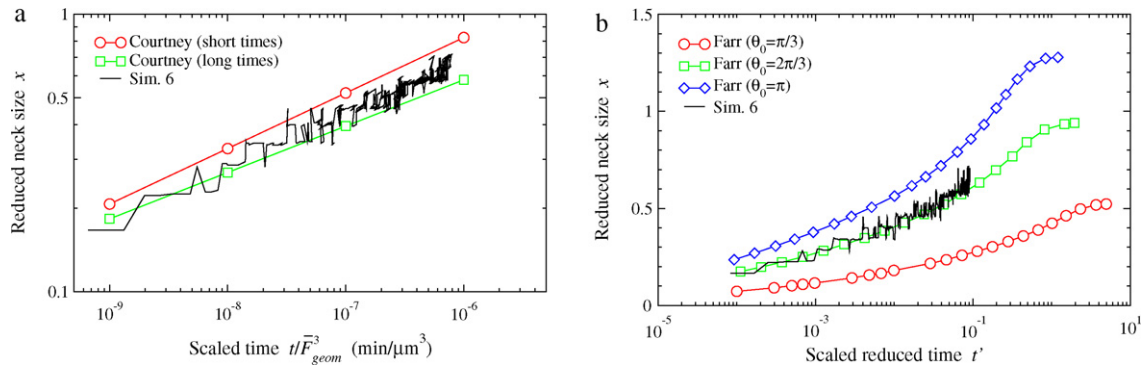


Fig. 12. Comparison of the neck growth curves predicted by the diffusional model with (a) those predicted by Courtney's theory [6], for early and late times, and (b) those predicted by Farr's theory [10], for different dihedral angles, θ_0 .

Courtney's predictions (early and late times). This indicates that this theory provides good fittings for neck growth in the diffusional model. On the other hand, Fig. 12b shows the evolution of the reduced neck size, x , with the scaled reduced time, t' , and the predictions, for different dihedral angles, corresponding to Farr's theory [10]. In this theory, t' is defined as

$$t' = \int_0^t \frac{k dt}{\bar{F}_{geom}^3} \quad (20)$$

where k is a temperature-dependent constant. According to Fig. 12b, the simulation result matches the prediction corresponding to $\theta_0 = 120^\circ$, at least for the simulated time (1000 MCS). However, note that no specific equilibrium dihedral angle has been introduced into the model and that, in absence of a grain boundary between the sintering particles, which is the case, θ_0 has to be equal to 180° . The good fitting with $\theta_0 = 120^\circ$ may be due to two reasons: (i) the short simulated time: the simulation is not at the late-time regime and, therefore, the system has not returned to equilibrium; and (ii) the insufficient resolution of the system: the parameter x_L equals $1 \mu\text{m}/\text{voxel}$ in this simulation and, hence, it may not allow to calculate the real value of θ_0 , which only has sense where the grain boundary, the particle surfaces and the liquid meet. What we may be catching here is the effect of the presence of Al and the so-called "zone of diffusion" surrounding the neck (note that Farr's theory [10] and the presented model do only include diffusion in the liquid, and not other diffusional mechanisms, such as surface or lattice-vacancy diffusion). As long as the neck is "sharp" ($x \leq 0.5$), the presence of Al impedes further solidification in the neck. Aluminium has to move away from that zone before more Si can solidify. At the same time, the neck has to grow in a way such that adequate Al diffusion away from the neck region is permitted. These processes set the neck growth and the particle shape in the region of the neck during the simulation, which are eventually captured by the parameter x as a function of t' . When both particles form a single spherical particle, which will only occur at late times, we will be able to calculate the real dihedral angle, $\theta_0 = 180^\circ$.

3.5. Simulations of complex microstructures

The final test for our diffusional model is to carry out simulations of complex systems. For this, we generate a system of $100 \mu\text{m} \times 100 \mu\text{m} \times 100 \mu\text{m}$, with $x_L = 1 \mu\text{m}/\text{voxel}$. We note that the system size is limited by the available computer speed and memory. For this reason, the simulated system has to be two orders of magnitude smaller than with the geometrical model ($10^6 \mu\text{m}^3$ vs. $1.25 \times 10^8 \mu\text{m}^3$). The calculation of c_{ave} and the diffusional process slow down the simulation dramatically.

We choose the initial size distribution to be bidisperse: 20 particles of $30 \mu\text{m}$ of diameter and 80 particles of $10 \mu\text{m}$ of diameter. This sets the initial average equivalent radius, \bar{R} , equal to $7 \mu\text{m}$, and $f_{vol} \simeq 30\%$. The particles are randomly placed in the system. They are allowed to overlap up to a maximum angle of 20° measured in the intersection of the overlapping particles. Fig. 13 shows the system configuration during the simulation. The liquid has been removed in Fig. 13a to ease the visualization of the particles.

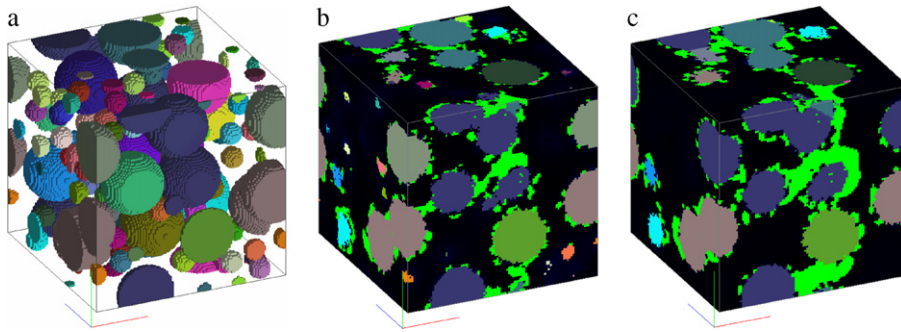


Fig. 13. Microstructural configuration of the complex system under study with the diffusional model: (a) at $t=0$, (b) $t=250$ MCS and (d) $t=1000$ MCS. In (a), liquid voxels have been removed for visualization purposes. Green voxels are supersaturated voxels ($c > 44\%$, w/w, Al). (For interpretation of the references to color in this figure legend, the reader is referred to the web version of the article.)

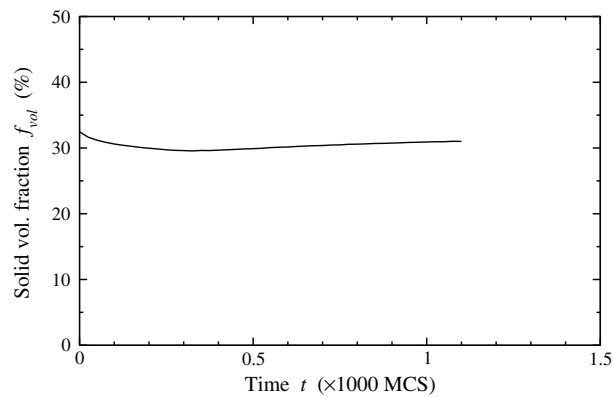


Fig. 14. Temporal evolution of the solid volume fraction, f_{vol} , in the complex system, simulated with the diffusional model.

Fig. 14 shows the temporal evolution of the solid volume fraction in the system. There is an initial stage in which the fraction of silicon of the system decreases. That initial stage lasts about 300 MCS. As we have mentioned, aluminium is initially homogeneously distributed in the system. However, according to Eq. (3), particles partially dissolve to reach the Si concentration of equilibrium at their surface. After that initial stage, some of the smaller particles are close to disappearing, as they have dissolved more, whereas some of the bigger particles are already growing and can form clusters or aggregates. Despite some clustering of the particles, if we treat them as separate, we can calculate \bar{R}

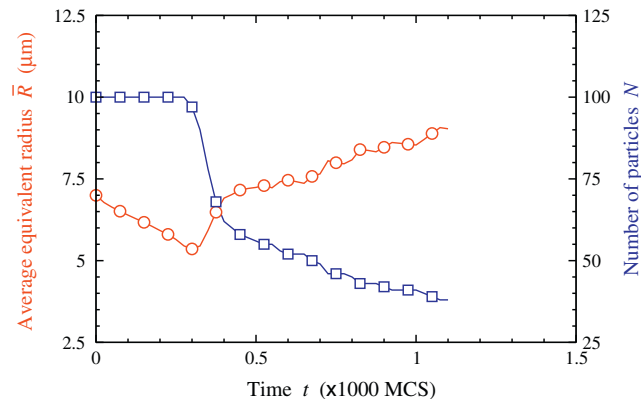


Fig. 15. Temporal evolution of the average equivalent radius, \bar{R} (circles), and the number of particles, N (squares), in the complex system, simulated with the diffusional model.

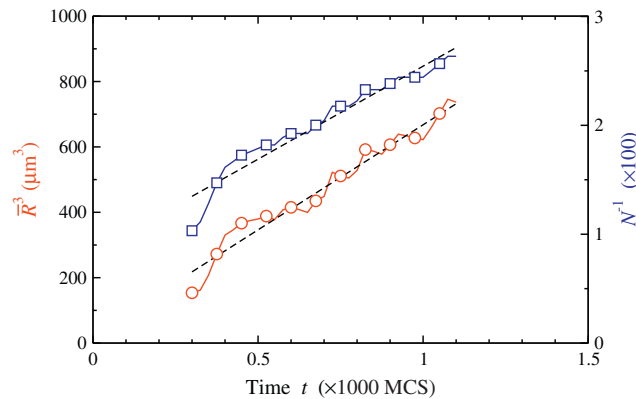


Fig. 16. Temporal evolution of \bar{R}^3 (circles) and N^{-1} (squares) in the complex system simulated with the diffusional model (diffusion-limited case).

from their volumes, as shown in Fig. 15. As we can observe in that figure, while the number of particles, N , decays significantly with time, the value of \bar{R} increases.

Fig. 16 shows \bar{R}^3 and N^{-1} as a function of t , for $t \geq 300$ MCS. The linear fit shown in that figure yields a ripening rate, κ , equal to $0.64 \mu\text{m}^3/\text{MCS}$, with a correlation coefficient of 97.9%. N^{-1} and t are also well correlated (97.1%). The obtained dependences between the studied variables, namely $\bar{R}^3 \propto t$ and $N^{-1} \propto t$, are precisely the relationships proposed by the LSW theory and other analytical theories (see the detailed review carried out by Baldan in Ref. [3]) for the diffusion-limited Ostwald ripening. Although the simulation is not in the scaling regime of particle sizes dealt by the LSW theory, this provides some evidence that the Ostwald ripening simulated with the present diffusional MC model is truly in the diffusion-limited regime.

Finally, in Fig. 17, we can observe the particle size distribution as a function of the reduced radius, $\zeta = R/\bar{R}$, at different times. Because of the initial bimodal distribution of particles, it is not possible to compare the attained distribution of particles with that predicted by the LSW theory. The short simulation time does not permit the particle distribution entering a self-similar regime. In addition, a finite volume fraction effect and the unusual size distribution (which is certainly not like the asymptotic scaling distribution of the LSW theory) contribute to the difference with respect to the LSW theory. However, we expect that the particle distribution will eventually evolve towards a monomodal distribution of particles of a similar shape as found by other authors for liquid phase sintering [3]. Unfortunately, there is no experimental evidence to compare with this simulation.

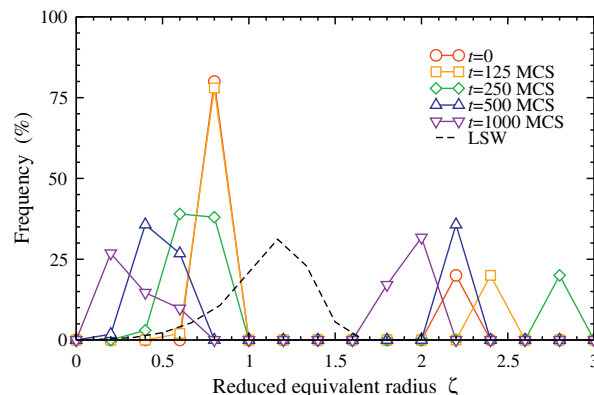


Fig. 17. Particle size distribution as a function of the reduced equivalent radius, ζ , at different times, in the complex system, simulated with the diffusional model.

4. Conclusions

We have developed a diffusional model, based on the Monte Carlo technique, for the microstructural evolution of liquid-solid systems, in which coarsening by Ostwald ripening and by particle coalescence can take place. The main advantages of this model compared to other models is that a second component and the diffusion of this component can be taken into account. Besides, because we are working with a discretised system, we can analyse the local behaviour of the model, which is an improvement with respect to obtaining the overall behaviour of the system, in terms of \bar{R} and N . The diffusional model presented in this work permits reproducing different regimes of Ostwald ripening, depending on value given to the dimensionless diffusion parameter \tilde{D} . The model has been obtained and then validated for the aluminium–silicon binary system at the temperature of 1375 K. But the procedure for obtaining the C-PDF is flexible enough so different materials (with the limitations indicated in this work) and a different temperature could be chosen. The simulation carried out starting with a complex microstructure yields an evolution of the mean radius and the number of particles with time as $\bar{R}^3 \propto t$ and $N^{-1} \propto t$, respectively. These results indicate that the simulations performed with the present diffusional MC model are in the diffusion-limited regime. However, due to the short simulation time, a self-similar regime has not been reached, yet. Besides, because of the occurrence of particle coalescence, which is not considered by the LSW theory, comparison with the asymptotic results of Lifshitz and Slyozov's theory for diffusion-limited Ostwald ripening in the zero volume-fraction limit is difficult. In this sense, the proposed model could be more easily compared with real systems, in which both Ostwald ripening and neck formation take place at the same time. Nevertheless, no experimental results have been found to compare with these simulations.

Acknowledgement

The authors would like to thank Unilever R&D Colworth (UK) for the support of this research.

References

- [1] J. Aldazabal, A. Martí-Meizoso, J.M. Martínez-Esnaola, Simulation of liquid-phase sintering using the Monte Carlo method, *Mater. Sci. Eng. A* 365 (2004) 151–155.
- [2] A.J. Ardell, The effect of volume fraction on particle coarsening: theoretical considerations, *Acta Metall.* 20 (1972) 61–71.
- [3] A. Baldan, Progress in Ostwald ripening theories and their application to nickel-base superalloys, *J. Mater. Sci.* 37 (2002) 2171–2202.
- [4] A.D. Brailsford, P. Wynblatt, The dependence of Ostwald ripening kinetics on particle volume fraction, *Acta Metall.* 27 (1979) 489–497.
- [5] C.J. Clarke, *The science of ice cream*, Royal Society of Chemistry, Cornwall, UK, 2004.
- [6] T.H. Courtney, A reanalysis of the kinetics of neck growth during liquid-phase sintering, *Metall. Trans. A* 8 (1977) 671–677.
- [7] T.H. Courtney, Microstructural evolution during liquid-phase sintering: development of microstructure, *Metall. Trans. A* 8 (1977) 679–684.
- [8] C.K.L. Davies, P. Nash, R.N. Stevens, The effect of volume fraction of precipitate on Ostwald ripening, *Acta Metall.* 28 (1980) 179–189.
- [9] Y. Enomoto, M. Tokuyama, K. Kawasaki, Finite volume fraction effects on Ostwald ripening, *Acta Metall.* 34 (1986) 2119–2128.
- [10] R.S. Farr, A. Luque, M.J. Izzard, M. van Ginkel, Liquid-phase sintering of two roughened ice crystals in sucrose solution: a comparison to theory and simulation, *Comput. Mater. Sci.* 44 (2008) 1135–1141.
- [11] A. Karma, W.J. Rappel, Quantitative phase-field modeling of dendritic growth in two and three dimensions, *Phys. Rev. E* 57 (1998) 4323–4349.
- [12] S.-B. Lee, J.M. Rickman, A.D. Rollett, Three-dimensional simulation of isotropic coarsening in liquid-phase sintering. I. A model, *Acta Mater.* 55 (2007) 615–626.
- [13] D.R. Lide, *CRC Handbook of Chemistry and Physics*, CRC Press, Florida, USA, 1992.
- [14] I.M. Lifshitz, V.V. Slyozov, The kinetics of precipitation from supersaturated solid solutions, *J. Phys. Chem. Solids* 19 (1961) 35–50.
- [15] A. Luque, J. Aldazabal, J.M. Martínez-Esnaola, A. Martí-Meizoso, J. Gil Sevillano, R.S. Farr, Geometrical Monte Carlo model of liquid-phase sintering, *Math. Comp. Simul.* 80 (2010) 1469–1486.
- [16] J.A. Marqusee, J. Ross, Theory of Ostwald ripening: competitive growth and its dependence on volume fraction, *J. Chem. Phys.* 80 (1984) 536–543.
- [17] A. Martí-Meizoso, J.M. Martínez-Esnaola, 3-D grain growth kinetics using Q-Potts models. Tetraikadehedron space discretisations, *Mater. Sci. Forum* 113 (1993) 361–366.
- [18] N. Metropolis, A.Si. Rosenbluth, M.N. Rosenbluth, A.H. Teller, E. Teller, Equation of state calculations by fast computing machines, *J. Chem. Phys.* 21 (1953) 1087–1092.
- [19] Si. Ostwald, Über die vermeintliche Isometrie des roten und gelben Quecksilberoxyds und die Oberflächenspannung fester Körper, *Z. Phys. Chem.* 34 (1900) 495–503.
- [20] P.J.P. Pimienta, E.J. Garboczi, Si.C. Carter, Cellular automaton algorithm for surface mass transport due to curvature gradients: Simulations of sintering, *Comp. Mater. Sci.* 1 (1992) 63–77.
- [21] Si.H. Press, S.A. Teukolsky, Si.T. Vetterling, B.P. Flannery, *Numerical Recipes in C*, Cambridge University Press, Cambridge, UK, 1992.

- [22] D.J. Rowenhorst, J.P. Kuang, K. Thornton, P.Si. Voorhees, Three-dimensional analysis of particle coarsening in high volume fraction solid-liquid mixtures, *Acta Mater.* 54 (2006) 2027–2039.
- [23] S. Sarian, H.Si. Weart, Kinetics of coarsening of spherical particles in a liquid matrix, *J. Appl. Phys.* 37 (1966) 1675–1681.
- [24] R.L. Sutton, I.D. Evans, J.F. Crilly, Modelling ice crystal coarsening in concentrated disperse food systems, *J. Food Sci.* 59 (1994) 1227–1233.
- [25] V. Tikare, J.D. Cawley, Numerical simulation of grain growth in liquid phase sintered materials. I. Model, *Acta Mater.* 46 (1998) 1333–1342.
- [26] V. Tikare, J.D. Cawley, Numerical simulation of grain growth in liquid phase sintered materials. II. Study of isotropic grain growth, *Acta Mater.* 46 (1998) 1343–1356.
- [27] M. Tokuyama, K. Kawasaki, Statistical-mechanical theory of coarsening of spherical droplets, *Physica A* 123 (1984) 386–411.
- [28] K. Tsumuraya, Y. Miyata, Coarsening models incorporating both diffusion geometry and volume fraction of particles, *Acta Metall.* 31 (1983) 437–452.
- [29] P.Si. Voorhees, M.E. Glicksman, Solution to the multi-particle diffusion problem with applications to Ostwald ripening. I. Theory, *Acta Metall.* 32 (1984) 2001–2011.
- [30] C. Wagner, Theorie der Alterung von Niederschlagen durch Umlosen (Ostwald Reifung), *Z. Electrochem.* 65 (1961) 581–591.
- [31] A.-M. Williamson, A. Lips, A. Clark, D. Hall, Late stage coarsening in concentrated ice systems, *Faraday Discuss.* 112 (1999) 31–49.
- [32] A.-M. Williamson, A. Lips, A. Clark, D. Hall, Ripening of faceted ice crystals, *Powder Technol.* 121 (2001) 74–80.
- [33] J.-H. Yao, K.R. Elder, H. Guo, M. Grant, Theory and simulation of Ostwald ripening, *Phys. Rev. B* 47 (1993) 14110–14125.